nature communications

Article

https://doi.org/10.1038/s41467-024-51523-2

Improving the creation of SiV centers in diamond via sub-μs pulsed annealing treatment

Received: 12 March 2023

Accepted: 9 August 2024

Published online: 23 August 2024

Check for updates

Yan-Kai Tzeng[1,11], Feng Ke[2,3,4,11], Chunjing Jia[2,5,11], Yayuan Liu[6], Sulgiye Park[3], Minkyung Han[3,6], Mungo Frost[7], Xinxin Cai[8], Wendy L. Mao[2,3], Rodney C. Ewing[3], Yi Cui[6], Thomas P. Devereaux[2,6], Yu Lin[2] ✉ & Steven Chu[1,9,10] ✉

Silicon-vacancy (SiV) centers in diamond are emerging as promising quantum emitters in applications such as quantum communication and quantum information processing. Here, we demonstrate a sub-μs pulsed annealing treatment that dramatically increases the photoluminescence of SiV centers in diamond. Using a silane-functionalized adamantane precursor and a laser-heated diamond anvil cell, the temperature and energy conditions required to form SiV centers in diamond were mapped out via an optical thermometry system with an accuracy of ±50 K and a 1 μs temporal resolution. Annealing scheme studies reveal that pulsed annealing can obviously minimize the migration of SiV centers out of the diamond lattice, and a 2.5-fold increase in the number of emitting centers was achieved using a series of 200-ns pulses at a 50 kHz repetition rate via acousto-optic modulation. Our study provides a novel pulsed annealing treatment approach to improve the efficiency of the creation of SiV centers in diamond.

Lattice defects that form optical impurity centers are ubiquitous in crystalline materials. Among these defects, color centers in diamond have emerged as promising platforms for a variety of applications in quantum communication[1,2], quantum photonics[3,4], and biological sciences[5,6]. While diamond has been demonstrated to host hundreds of impurity color centers[7], very few such color centers have been well characterized. The most studied color centers in diamond are nitrogen-vacancy (NV)[8,9] and SiV[10,11] defects, which have drastically different optical properties. The NV color center has the quantum property of electron spin with a long coherence time at room temperature. This electron spin can be prepared optically and then manipulated using optical, magnetic, and radiofrequency techniques[12,13]. Even so, using the NV center as a single-photon source has two main drawbacks: (1) only about 4% emission light in the zero-phonon line (ZPL) and (2) an electric dipole moment that generates strong inhomogeneous broadening of the spectral line[14]. By comparison, the SiV center consisting of one silicon atom located halfway between two empty lattice sites has an inversion symmetry and no dipole moment. It shows great promise as a single-photon source, as it has a narrow ZPL (a large Debye-Waller factor) of 70%, a high photon

[1]Department of Physics, Stanford University, Stanford, California 94305, USA. [2]Stanford Institute for Materials and Energy Sciences, SLAC National Accelerator Laboratory, Menlo Park, California 94025, USA. [3]Department of Earth and Planetary Sciences, Stanford University, Stanford, California 94305, USA. [4]State Key Laboratory of Metastable Materials Science and Technology, Yanshan University, 066004 Qinhuangdao, Hebei, China. [5]Department of Physics, University of Florida, Gainesville, FL 32608, USA. [6]Department of Materials Science and Engineering, Stanford University, Stanford, California 94305, USA. [7]SLAC National Accelerator Laboratory, Menlo Park, California 94025, USA. [8]Department of Physics and Astrophysics, University of Rochester, Rochester, New York 14627, USA. [9]Department of Molecular and Cellular Physiology, Stanford University, Stanford, California 94305, USA. [10]Department of Energy Science and Engineering, Stanford University, Stanford, California 94305, USA. [11]These authors contributed equally: Yan-Kai Tzeng, Feng Ke, Chunjing Jia. ✉e-mail: lyforest@slac.stanford.edu; schu@stanford.edu

emission rate (short excited-state lifetime at room temperature), and near-infrared emission (ZPL at 738 nm)[15]. These optical properties of the SiV center make it ideal for narrow-band photonic devices, including cavity and waveguides[3], and for the application as a single-photon emitter[16].

Two approaches have been widely employed for fabricating SiV centers in diamond, ion implantation[15,17] and chemical vapor deposition (CVD) techniques[10,18]. Besides implantation and CVD, high-pressure and high-temperature (HPHT) methods using a laser-heated diamond anvil cell (DAC) have been previously employed to synthesize nanodiamonds, allowing the doping of nanodiamonds with SiV centers using tetraethylorthosilicate precursors[19–21].

Ion implantation using a focused ion beam is a widely available commercial approach. However, it induces extensive structural damage, and a sequence of high-temperature annealing treatment in vacuum after ion implantation is required. Furthermore, the conversion of the implanted silicon ions to SiV centers is far less efficient than that of the nitrogen ions to NV centers[15,17] due to their structural differences. Compared with the structure of the NV center which consists of a substitutional nitrogen atom adjacent to a lattice vacancy, the size of the silicon atom is too large (~1.5 times as large as nitrogen) to replace a carbon atom at a diamond lattice site.

The current solution for enhancing the conversion efficiency of implanted silicon ions into SiV centers involves increasing the number of vacancies via additional electron irradiation. However, this method concomitantly creates additional damage in the diamond lattice[22]. Alternatively, CVD technology enables the synthesis of high-quality diamonds with the desired doping atoms using an ionic plasma, but the ionic plasma makes it difficult to control the high-temperature growth environment. In addition, neither of the two methods allows us to fully understand the color center introduction and vacancy migration processes in situ. Comprehending the optimal methods for creating and subsequently stabilizing SiV color centers within the diamond lattice could enhance the brightness of these color centers. In pursuit of this objective, this work offers fundamental thermodynamic and kinetic insights into the formation mechanism of luminescent color centers through the combination of Si ions and vacancies. Here, we present the first mechanistic study on the formation of SiV centers in diamond using temporally controlled annealing. Additionally, we devise a novel annealing scheme for improving the conversion efficiency, which can serve as a guiding framework for the synthesis of numerous other color centers of interest.

Synthesis of SiV centers in diamond

In this study, we performed a direct synthesis of SiV centers in diamond from a silicon-containing adamantane precursor (adamantylethyltrichlorosilane, AdaSi) using an HPHT approach via a laser-heated DAC[23–25]. The laser-heated DAC described in this work offers several advantages over ion implantation and CVD including the ability to map out the temperature and pressure conditions necessary for the formation of SiV from AdaSi and the ability to explore a variety of different growth and annealing conditions in the same DAC. In addition, the transparency of the diamond window allows penetration of both the continuous wave (CW) and pulsed laser for precise annealing control, and in situ measurements of the sample temperature and pressure. Pressure was calibrated at room temperature by monitoring the spectral shift of the R-line fluorescence (694.25 nm) from a ruby ball[24] inside the sample chamber and Raman shift of the diamond peak at 1332 cm^{-1} from the diamond window. Since the DAC was under applied stress, the first-order Raman peak of diamond resulted in the blue shift of the diamond Raman peak[26].

Adamantane has been documented to be a superior precursor material for laser-induced HPHT diamond synthesis[23]. Nitrogen-functionalized adamantane has also been shown to convert to fluorescent diamonds at high pressure and moderate temperature[27], validating the use of AdaSi for the synthesis of SiV emitting centers in diamond. In order to ensure homogeneous coupling between AdaSi and the laser absorber and reproduce a uniform laser power versus temperature profile across the entire sample chamber, all experiments were performed on a sandwiched sample stack where a 100-nm-thick tungsten layer as the laser absorber is deposited on top of a mica layer that is sandwiched between AdaSi. This sandwich geometry allows a 1064 nm Nd:YLF laser to uniformly heat AdaSi followed by annealing of the converted diamond, as illustrated in Fig. 1.

To elucidate the formation and migration dynamics of SiV centers in diamond, we developed a controlled laser-heating apparatus in which high temperature is realized via the metal absorption of the Nd:YLF laser radiation. The temporal control of heating is accomplished by an acousto-optic modulator (AOM) to switch the CW laser into short pulses of light focused onto the tungsten film deposited on a mica substrate inside the DAC (Fig. 1 and Supplementary Fig. 1). Temporal resolution of the laser heating is directly correlated to the rise/fall time of the AOM that is on the timescale of 150 ns (Supplementary Fig. 2). Using our system, ultrafast heating at 0.1 GK/s and cooling at 0.1 MK/s can be achieved (Supplementary Fig. 3).

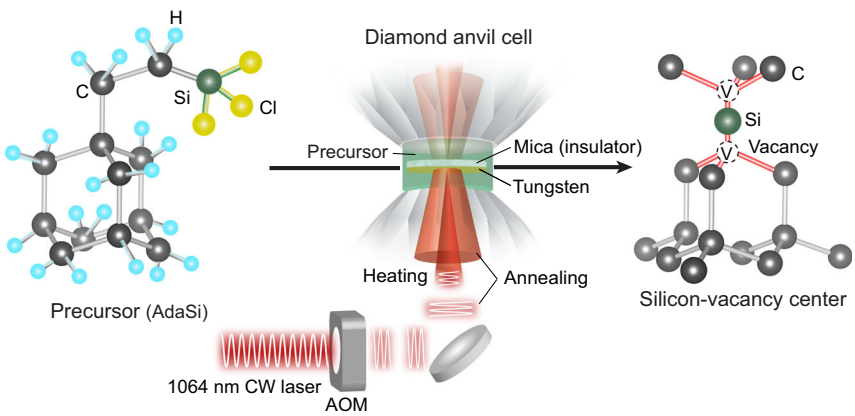

Fig. 1 | Schematic illustration of pulsed laser-heating and annealing system. A schematic illustration of our annealing concept for improving SiV centers in diamond and the experimental setup of the laser-heating system. AOM-modulated pulsed lasers utilized as the heating and annealing laser deposit sufficient energy to induce diamond material conversion in a time comparable to or shorter than the period of SiV centers migrating out of the diamond lattice. AdaSi is the precursor to form diamond with SiV centers. C, gray; Si, green; Cl, yellow; H, cyan. Local heating and annealing were achieved by laser irradiating the 100-nm-thick tungsten film deposited on mica.

https://doi.org/10.1038/s41467-024-51523-2

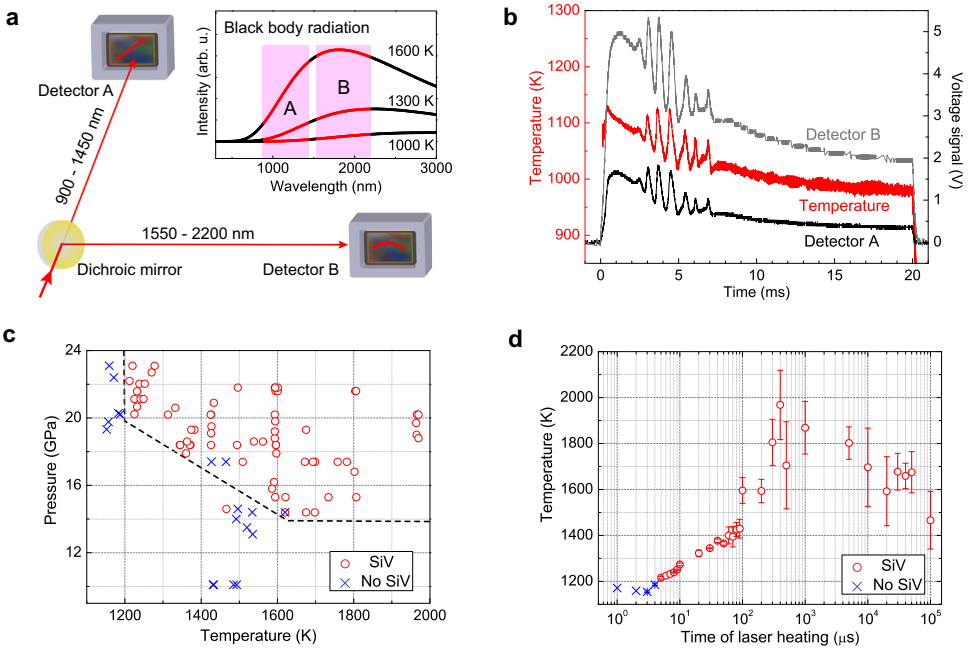

Fig. 2 | In situ temperature measurement for laser-heated DAC. a A schematic illustration of the ultrafast thermometry setup. Instead of measuring the entire thermal radiation spectra, the integrated intensity ratio of two radiation windows, A: 900–1450 nm and B: 1550–2200 nm, was used for the temperature measurement. **b** Temperature (red curve) has been calibrated based on the ratio (windows: B/A) of the intensities recorded by two detectors (gray and black curves). The temperature curve was measured with 1-μs temporal resolution. Temperature oscillations displayed between 2 and 7 ms might be due to a phase transition of the tungsten metal. **c** A pressure-temperature synthesis diagram of SiV-containing diamond is shown with red circles and blue crosses representing the formation of SiV and no formation of SiV, respectively. Dashed lines indicate the phase boundary for the formation of SiV, as evidenced by the PL peak of SiV's ZPL. **d** At 18.4 GPa, with a laser intensity of 33 MW/cm^2 and a beam spot of 2.5 μm (FWHM), a 5-μs induction time was observed for the formation of the SiV center, which equals an energy fluence of 0.165 kJ/cm^2. After heating for 500 μs, the error bar of the temperature measurements becomes large due to temperature oscillations. The temperature error bars are from the fitting of the data.

We also implemented a simple and accurate thermometry system with 1 μs temporal resolution, which allows the determination of the precise temperature when AdaSi is converted to SiV-containing diamond at varying pressures. Typically, the temperature in the laser-heated DAC is determined by fitting the thermal radiation spectrum to the Planck radiation function. Instead of measuring the entire thermal radiation spectrum[22], two different radiation windows of 900–1450 nm and 1550–2200 nm are selected. The intensity ratio of the two ranges is then converted to determine temperatures above 1000 K (Fig. 2a, and Supplementary Figs. 1 and 4)[25]. Note that below 1000 K, the photodetector for 900–1450 nm is not sensitive enough to detect the radiation with negligible light being emitted. Filament lamps with a blackbody pyrometer were used to calibrate the optical intensities of the two photodetectors back to the experimental temperature. Temperature can be measured with a time resolution of better than 1 μs which is limited by the bandwidth of the photodetectors (Supplementary Fig. 5). The absolute accuracy of our ultrafast thermometer is estimated to be ±50 K (Fig. 2a and Supplementary Fig. 4).

Examples of detailed temperature response along heating and cooling are shown in Fig. 2b and Supplementary Fig. 3, with the widths of laser pulse heating being 20 ms and 10 μs, respectively. Interestingly, we observe clear temperature oscillations with time in certain temperature curves, which might be due to the melting/resolidification of the tungsten metal. The tungsten thin film was deposited via DC-magnetron sputtering. Despite producing a highly dense film, this method falls short of achieving a film with single-crystalline quality[28]. The melting temperature of a 100-nm-thick film containing tungsten atom-aggregation particles would be significantly lower than the reported melting temperature of a bulk tungsten sample[29]. We conjecture that the melted tungsten in this central region flows to the immediate surrounding region and resolidifies. The heat of fusion released plus the additional heat added by the laser pulse causes additional melting and cooling in this region. The temperature in these regions increases until additional melting occurs, which causes another round of cooling. During this time, additional heat continues to be deposited in the center of the focal spot so that multiple rounds of solidification and reheating occur. As a consequence, tungsten migrates away from the hottest, central area, as evidenced by clear thinning and eventual depletion of tungsten in the central region. This also explains why the temperature peaks at a pulse width of ~1 ms and is lower for pulses up to tens of microseconds (Fig. 2b). Meanwhile, AdaSi may undergo melting at high temperature and high pressure, making a non-negligible contribution to the observed temperature oscillations.

We recorded the highest temperature for constructing the pressure-temperature synthesis diagram where AdaSi transforms to diamond with SiV centers (Fig. 2c). The diamond formed from AdaSi showed a clear photoluminescence (PL) signal characteristic of SiV's ZPL. The PL of the SiV center, induced by a 514-nm excitation laser, was measured using an optical spectrometer and showed a linear blue shift upon compression (Supplementary Fig. 6), consistent with the reported theoretical results[19]. Since the SiV-containing diamond was produced in a laser-heated DAC, the characterization of the diamond quality was performed ex situ. After fully releasing pressure, the retained diamond samples can be well characterized using scanning electron microscopy (SEM), Raman spectroscopy, and SEM/energy dispersive spectroscopy analysis (Supplementary Figs. 7–11). The PL peaks of previously reported[30–33] hydrogen-, nitrogen-, and tungsten-bearing vacancy centers are not observed in our study (Supplementary Fig. 9), suggesting that any inclusions of these centers, if present, are likely below the detection sensitivity of the equipment used in our experiments. Furthermore, the Raman results reveal that many C-H

https://doi.org/10.1038/s41467-024-51523-2

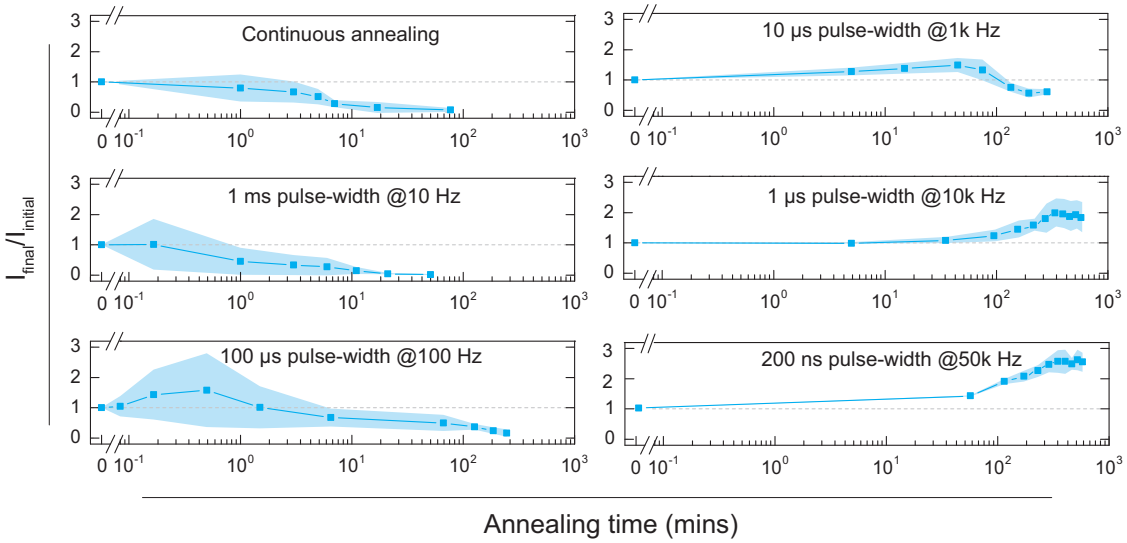

Fig. 3 | Sub-µs pulsed annealing measurement. Comparison of annealing with CW and pulsed lasers in a laser-heated DAC. Values above the dashed gray lines represent the results of increased SiV's PL intensity after laser annealing, i.e., the final intensity is higher than the initial value ($I_{final}/I_{initial} \geq 1$). The CW laser annealing shows a reduction of the PL intensity from the SiV's peak. After annealing for 350 min, the intensity of SiV's peak is close to zero. Each blue square represents the mean of the ratio of the intensity after annealing (I_{final}) divided by the intensity before annealing ($I_{initial}$), calculated across three sampling points. Pulsed annealing treatment was operated on different laser pulse repetition frequencies at 10, 100, 1k, 10k, 50k Hz with the corresponding 1k, 100, 10, 1 µs, 200 ns pulse width, using the same laser intensity of 260 kW/cm^2. Except the frequency of 10 Hz with 1 ms pulse width, pulsed annealing with higher repetition frequencies shows increasing SiV's PL in a nascent condition. In particular, at 50k Hz with 200 ns pulse width, SiV's PL enhances to 250% and does not show any visible decay after 10 h of pulsed annealing. For pulsed annealing measurements, each data point represents the mean of the ratio of $I_{final}/I_{initial}$ and the mean of two sampling points. Error bars (shaded light blue) represent one standard deviation from the mean.

bonds are disrupted (Supplementary Fig. 10). If hydrogen-related species were to form, they could diffuse throughout the lattice, potentially becoming trapped within or released out of the diamond crystals[34], as observed in previous studies involving argon and other elements[19,35].

By varying the pulse length of the AOM-switched laser beam and simultaneously recording the emission spectra of laser-heated spots, the laser energy required to form SiV was estimated to be above a threshold value of 0.18 kJ/cm^2 (Supplementary Figs. 12–14; Supplementary Table 1) at 18 – 20 GPa. For example, at 18.4 GPa with the laser intensity of 33 MW/cm^2 and a beam spot of 2.5 µm full-width at half-maximum (FWHM), we observed a 5-µs induction time (Supplementary Fig. 12) for the formation of SiV centers (Fig. 2d) which equals an energy fluence of 0.165 kJ/cm^2. Similarly, at 19.5 GPa with 0.5 MW/cm^2 and a 21.5-µm beam spot (FWHM), the delivery time was 200 µs and the energy is equivalent to 0.100 kJ/cm^2. At 18.4 GPa, using a nanosecond pulsed laser, the energy delivered by a ~5 µm beam at the peak energy of 25 µJ with a 5-ns pulse width was 0.176 kJ/cm^2 (Supplementary Fig. 14).

Sub-µs pulsed thermal annealing treatment

After the conversion of AdaSi to diamond with SiV centers, the as-formed diamond crystals would present many disordered carbon phases and especially unpaired silicon and vacancy. An annealing process is needed to stabilize and further increase SiV concentrations while reducing unwanted defects in diamond. We thermally annealed the diamond crystals by irradiating a larger area of the tungsten film with a CW laser focused with an apochromatic objective lens (Fig. 1 and Supplementary Fig. 1). An annealing laser beam of 21.5 µm in diameter (FWHM) was used to surround the photoluminescent diamond particles which were synthesized via laser heating a 2.5 µm sample spot in the DAC at 18 GPa. To avoid the melting of the tungsten thin film, we lowered the intensity of the Nd:YLF laser to 260 kW/cm^2. The ratio of SiV's PL intensity after the CW laser annealing to the initial value decreased quickly as a function of annealing time and dropped to zero with a decay time of ~180 s at half-maximum intensity (Fig. 3a), suggesting that the CW annealing treatment with a long annealing time is not suitable for stabilizing SiV centers in the diamond lattice.

An unstable SiV defect center would eventually anneal to the surface of the diamond crystals once the activation temperature that allows its mobility was achieved (e.g., at ~1000 K)[36]. Notably, the PL intensity showed an approximate 20% drop after the first 10-second annealing (Fig. 3a). This implies that a common thermal annealing technique[37] with a timescale of seconds may allow unstable SiV centers to migrate to a surface or grain boundaries. We conjecture that very short annealing times may lower the probability of migration of SiV centers to the surface of the crystals while still allowing SiV centers to form.

For this reason, we investigated sub-µs pulsed thermal annealing. The AOM-modulated laser was operated on different pulse repetition frequencies and pulse widths. A set of pulse repetition frequencies at 10, 100, 1k, 10k, 50k Hz with the corresponding 1k, 100, 10, 1 µs, 200 ns pulse width was used to produce the same laser intensity of 260 kW/cm^2 at 18 GPa. Figure 3 plots the ratio of the SiV's PL intensity after the pulsed annealing treatment to the starting intensity ($I_{final}/I_{initial}$) as a function of annealing time.

Pulsed annealing treatment with a pulse width of 200 ns is found to enhance SiV's PL intensity up to 250%. However, continued pulsed annealing treatment with a pulse width of 100 and 10 µs results in the decrease of PL to half of its intensity at 2 and 125 min, respectively. Interestingly, for the 100-µs pulsed annealing, the PL intensity increases to 150% in the first 30 s and then drops close to zero at 4 h. For the 10-µs pulse width (Supplementary Fig. 15), SiV's PL intensity also increases to 150% after annealing 50 min and then decreases to 50% beyond which the intensity remains constant with increasing pulsed annealing time.

SiV's PL keeps increasing to 200% under annealing with the 1-µs pulse width. With the 200-ns pulse width annealing treatment, SiV's PL

https://doi.org/10.1038/s41467-024-51523-2

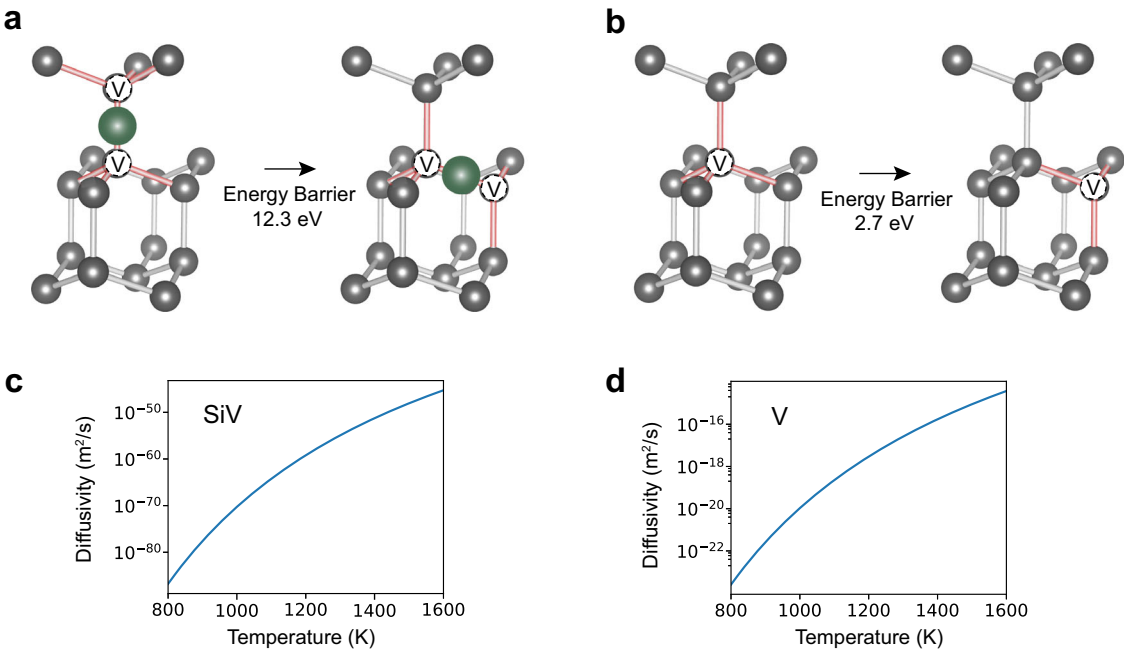

Fig. 4 | Calculated diffusion pathways, energy barriers, and diffusivity for SiV and vacancy. a The diffusion pathway and NEB calculated energy barrier for SiV. **b** The diffusion pathway and NEB calculated energy barrier for vacancy. **c** Calculated diffusivity for SiV diffusion. **d** Calculated diffusivity for vacancy diffusion.

shows the same rising trend as that with the 1 µs pulse width and SiV's intensity increases to 250%. Significantly, the PL intensities with laser pulse widths of both 1 µs and 200 ns do not show any visible decay after 10 h of pulsed annealing. Simultaneously, the ZPL peak of SiV centers gradually becomes narrower as the diamond quality improves with pulsed annealing (Supplementary Fig. 16).

Simulations of SiV and vacancy diffusion dynamics

To further understand the SiV and vacancy diffusion dynamics, we performed nudged elastic band (NEB)[38,39] calculations. In the NEB method, the minimum activation energy for chemical/physical processes can be obtained by constructing a series of fictitious intermediate transition states connecting the initial and final states and searching for the energy saddle point and the corresponding three-dimensional structure for the minimum energy path. We prepared the initial and final states by enumerating all the "irreducible" diffusion pathways at the microscopic scale and found the pathways for SiV and vacancies with the lowest energy barriers, as shown in the schematic plots of Fig. 4a, b, and Supplementary Figs. 17 and 18.

The initial and final state configurations of SiV and vacancies were optimized by relaxing all the internal atomic positions in the 2 × 2 × 2 supercell (64 carbon atoms without the SiV center) using density functional theory (DFT). NEB calculations, as implemented in Vienna Ab initio Simulation Package (VASP)[40–43], were then performed for these pathways and the total energies of the initial, intermediate, and final states for a transition pathway would tell us the energy barrier for the microscopic diffusion process (Supplementary Fig. 19). As shown in Fig. 4a, b, and Supplementary Fig. 16, the lowest diffusion energy barrier for the SiV center is 12.3 eV, while the lowest diffusion energy for vacancy is 2.7 eV, an order of magnitude lower.

We further applied the transition rate theory to calculate the corresponding diffusivity D for SiV and vacancy. The diffusivity can be calculated by $D = \upsilon_0 d^2 \exp(-\frac{\Delta E}{k_B T})$,

in which υ_0 is the attempted diffusion frequency, d is the distance of each diffusion step, and ΔE is the diffusion energy barrier[44,45].

As shown in Fig. 4c, d, theoretical calculations suggest that an isolated vacancy has a diffusivity many orders of magnitude higher than SiV in the diamond crystals from 800 to 1600 K. This huge diffusivity difference mainly arises from the huge difference in the energy barriers of these two defects. This result indicates that isolated vacancies can diffuse much faster than a SiV center in the diamond lattice under higher-temperature annealing. Under these conditions, vacancies uncoupled to Si impurities are much more likely to diffuse to the surface of the crystals while the SiV center remains stabilized in the diamond lattice. Although NEB calculations and theoretical diffusivity calculations were performed at ambient pressure, we expect that the relationship between SiV and vacancy diffusion would extend to high pressure since the lattice constant of diamond is rather robust up to tens of GPa.

Conclusions

In summary, we investigated the dynamics associated with the creation and stabilization of SiV centers in diamond via an AOM-modulated laser-heated DAC. We developed a µs-timescale thermometer for precise temperature measurements in situ. At 20 GPa, the minimum temperature needed to form SiV centers in diamond from the AdaSi precursor was 1200 K. Taking advantage of an AOM system that offers high temporal resolution up to tens of nanoseconds, we have elucidated the creation processes of SiV centers in diamond and determined the formation energy (0.18 kJ/cm^2).

Our combined theoretical and experimental results demonstrate that SiV centers can be stabilized while the crystalline quality of as-formed diamonds improves during the creation of artificial SiV centers. The ultra-short pulse annealing strategy allows the formation of additional optically active SiV centers while limiting the diffusion of SiV defects. By means of a sequence of pulsed annealing treatment with a 200-ns pulse width at 50k Hz, the concentration of SiV centers in diamond increased to 250% of its initial value and remained invariant after several hours of annealing. Our approach to annealing diamond with SiV centers may be applicable to other impurity-vacancy structural defects in diamond, particularly those associated with group IV or V elements.

More generally, the iterative application of rapid pulsed-laser annealing, combined with optimization of time and temperature annealing conditions, could be used to improve both the luminescent and electronic properties across various condensed matter materials

such as perovskite solar cells[46] and transition metal dichalcogenide-based transistors[47].

Methods

Sample preparation

AdaSi (95% purity, purchased from Gelest Inc.) was loaded on the top of a substrate, which is a 100-nm thin film of tungsten deposited by sputtering (Kur J. Lesker company) upon an exfoliated fluorine mica (Changchun Taiyuan fluorophlogopite Co. Ltd) of 150 × 150 × 1 μm. Because of the high melting point (3422 °C) of tungsten, it is not easy for the thin film to melt during the annealing process which serves as the absorber of light. The uniform tungsten results in the repeatability of laser-induced temperatures throughout experiments, compared to the mixture of samples with gold nanoparticles. Here, AdaSi is not only the seeding sample but also the pressure-transmitting medium without any other additive. The sample loading in the DAC was done at atmospheric pressure and clean environment.

Preparation of a DAC

High pressure was generated from a Mao-Bell-type symmetric DAC with diamond culets of 500 μm in diameter (purchased from Almax easyLab Inc.). A 301 stainless steel sheet with a thickness of 250 μm was used as the gasket. The gasket was initially indented to a thickness of 40 μm, and then a hole with a diameter of 295 μm was drilled at the center of the indented area using an electrical discharge machining machine, thus creating the sample chamber. Pressure in the sample chamber was calibrated by monitoring the spectral shift of the R-line fluorescence from a small ruby ball (Betsa Company, France) or the Raman peak shift of diamond.

Experimental setup

The laser-heated DAC system with temperature measurement is shown in Supplementary Fig. 1. The Nd:YLF CW laser (IPG PHOTONICS) is aligned with the AOM to produce a pulse mode laser. The acoustic wave within the crystal is powered by a 2 W, 110 MHz RF source (Model ME-1102T, IntraAction Corp.). The modulation is controlled via a waveform generator (33600 A Series, Agilent), and the resulting laser pulses have a rise time of ~150 ns. The AOM-modulated laser is focused onto the DAC sample through either one long working distance objective (M Plan Apo NIR, f = 200 mm, NA = 0.4, Mitutoyo) as the heating laser or an air-lens objective (N3437, Apochromat, f = 77 mm, F4.0, U.S. Laser Corporation) as the annealing laser. For temperature measurement, the blackbody radiation is collected through the long working distance objective, one 45° notch filter DM1 (NFD01-1064-25×36, Semrock), and one 0° notch emission filter at 1064 nm. And then the radiation is separated into two by a short-pass filter DM2 (DMSP1500, Thorlabs), one with a wavelength ranging from 900 to 1450 nm detected by the InGaAs photodetector (DET10N2, Thorlabs) and the other one from 1550 to 2200 nm detected by the air-cooling photodetector (PDA10DT, Thorlabs). These two photodetectors are calibrated for different temperature ranges. For temperature calibration, we use a homemade blackbody source to generate the blackbody radiation and measure its temperature via a pyrometer. Our ultrafast thermometry method can easily capture the changes in temperature occurring from hundreds of nanoseconds to microseconds, the time resolution of which is limited by the rising time of the photodetector.

PL measurements

The PL intensity was collected from the samples in the DAC via a long working distance objective (24 mm working distance, 20x/0.35NA SLWD EPI Objective, Nikon) using a Renishaw inVia Raman (spectral resolution: 2–4 cm^{-1}) system in Extreme Environments Laboratory at Stanford University (λ = 514.5 nm). A laser power of about 5 mW and an exposure time of 5 s per measurement were used. The PL spectra as a function of pressure were obtained by compressing the samples at room temperature.

Raman spectroscopy measurements

Raman spectra were collected using a Horiba LabRam HR Evolution Raman system at the Stanford Nano Shared Facilities (SNSF). A laser excitation wavelength of 532 nm was utilized. A power of 0.5 mW was kept throughout the measurements to avoid the potential laser-induced heating on the samples. Three accumulations with an exposure time of 10 s per accumulation were conducted to obtain a good Raman spectrum. Before the measurements, the Raman system was calibrated using the Raman mode of silicon at 520 cm^{-1}.

Simulation method

NEB[48] is a method to calculate the activation energy for chemical/physical processes by constructing a series of intermediate transition states, which we refer to as "image states." They connect two potential energy minima (the initial and final states). By optimizing the path or employing the "elastic band" anchored on endpoints and allowing intermediate transition states to relax, we can obtain an optimized activation energy barrier.

The NEB calculations were done in the framework of ab initio DFT as implemented in VASP version 6[40]. A supercell of diamond with 64 carbon atoms with periodic boundary conditions was used as the starting structure. The initial and final state configurations with SiV and V were calculated by relaxing all the internal atomic positions in the supercell. The SiV center has a negative charge, so strictly speaking we calculated SiV^-. The V center has zero charge, which can also be denoted as V^0. Spin-polarized calculations were performed. We found that the position relaxation of the atoms up to 2 and 3 atoms away from the SiV color center can make non-negligible contributions to the total energy. For this reason, all the atomic positions in the supercell were relaxed rather than just relaxing the atoms right next to SiV or V.

To study the SiV and V diffusion dynamics, all the "irreducible" diffusion pathways at the microscopic scale were enumerated. Specifically, the initial and final states are shown in the schematic plots of Supplementary Fig. 17. All the longer-range pathways can be decomposed into combinations of these pathways. The NEB calculations were then performed with four intermediate image states, in which the atomic positions are obtained by a linear interpolation between the initial and final state structures along these pathways and −5 spring constant as implemented in VASP.

To construct the image states, we started with relaxing only a limited number of atoms right next to the SiV color center as the test runs, moving and finally relaxing all the atoms in the supercell in the calculations. For the same reason as the equilibrium state configurations, we found that relaxing all atoms resulted in a significant change to the calculated total energy. Finally, the fitted total energies of the initial, four images, and final states were found using 1D cubic interpolation as implemented in scipy[49]. The fitted energy barrier curves for the different pathways are shown in Supplementary Fig. 17. The initial, intermediates and final states configurations corresponding to the SiV diffusion pathway PW1 have been shown in Supplementary Fig. 18.

A more detailed study for SiV and vacancy pathways for the nearest-neighbor hopping was used to identify the lowest transition energy barriers of all the irreducible pathways. Specifically, NEB calculations were performed for the nearest-neighbor transitions with nine intermediate states using the previous NEB intermediate state structures (four intermediate states) as the starting points. The converged NEB calculations show the transition energy barrier ΔE = 12.3 eV for SiV and ΔE = 2.7 eV for vacancy, as shown in Supplementary Fig. 19.

The diffusivity is further calculated using the expression for thermally activated diffusion, $D = \upsilon_0 d^2 \exp\left(-\frac{\Delta E}{k_B T}\right)$, where υ_O is the attempted diffusion frequency, d is the distance of each diffusion step, and ΔE is the diffusion energy barrier. The attempted diffusion

frequency[44,50,51] can be calculated as

$$\upsilon_0 = \frac{k_B T}{h} \prod_{j=1}^{m'} \frac{\exp\left(-\frac{h\upsilon_j^{TS}}{2k_B T}\right)}{1-\exp\left(-\frac{h\upsilon_j^{TS}}{k_B T}\right)} \left(\prod_{j=1}^{m} \frac{\exp\left(-\frac{h\upsilon_j^{IS}}{2k_B T}\right)}{1-\exp\left(-\frac{h\upsilon_j^{IS}}{k_B T}\right)} \right)^{-1} \quad (1)$$

where m and υ^{IS} are the number of normal modes and their frequencies for the initial state, and m' and υ^{TS} are the number of normal modes and their frequencies for the transition state or state at the saddle point.

The normal phonon modes were calculated for the initial and transition states that were obtained from previous NEB calculations using VASP. The structures at the saddle points for both SiV and vacancy nearest-neighbor hopping were obtained. Then normal phonon modes using a finite difference method have been implemented using VASP for the initial (final) states as well as the intermediate states for the saddle points for both SiV and vacancy diffusion. Please note that the number of normal phonon modes for vacancy obeys the relation $m' = m - 1$ for vacancy and $m' = m - 3$ for SiV. The three unstable phonon modes for SiV in the saddle point structure correspond to the three degrees of freedom for the composite SiV impurity, which is composed of one Si atom and two C vacancies, along the diffusion direction.

Reporting summary

Further information on research design is available in the Nature Research Reporting Summary linked to this article.

Data availability

All data generated or analyzed during this study are included in this article and its supplementary information files. Additional data that support the findings of this study are available from the corresponding authors upon request.

References

1. Bhaskar, M. K. et al. Experimental demonstration of memory-enhanced quantum communication. *Nature* **580**, 60–64 (2020).
2. Evans, R. E. et al. Photon-mediated interactions between quantum emitters in a diamond nanocavity. *Science* **362**, 662–665 (2018).
3. Radulaski, M. et al. Nanodiamond integration with photonic devices. *Laser Photonics Rev.* **13**, 1800316 (2019).
4. Aharonovich, I., Greentree, A. D. & Prawer, S. Diamond photonics. *Nat. Photonics* **5**, 397–405 (2011).
5. Wu, Y., Jelezko, F., Plenio, M. B. & Weil, T. Diamond quantum devices in biology. *Angew. Chem. Int. Ed. Engl.* **55**, 6586–6598 (2016).
6. Wu, T. J. et al. Tracking the engraftment and regenerative capabilities of transplanted lung stem cells using fluorescent nanodiamonds. *Nat. Nanotechnol.* **8**, 682–689 (2013).
7. Zaitsev, A. M. *Optical Properties Of Diamond* (Springer, 2001).
8. Gruber, A. et al. Scanning confocal optical microscopy and magnetic resonance on single defect centers. *Science* **276**, 2012–2014 (1997).
9. Gaebel, T. et al. Room-temperature coherent coupling of single spins in diamond. *Nat. Phys.* **2**, 408–413 (2006).
10. Neu, E. et al. Single photon emission from silicon-vacancy colour centres in chemical vapour deposition nano-diamonds on iridium. *New J. Phys.* **13**, 025012 (2011).
11. Sipahigil, A. et al. Indistinguishable photons from separated silicon-vacancy centers in diamond. *Phys. Rev. Lett.* **113**, 113602 (2014).
12. Maze, J. R. et al. Nanoscale magnetic sensing with an individual electronic spin in diamond. *Nature* **455**, 644–647 (2008).
13. Balasubramanian, G. et al. Nanoscale imaging magnetometry with diamond spins under ambient conditions. *Nature* **455**, 648–651 (2008).
14. Jelezko, F. et al. Spectroscopy of single N-V centers in diamond. *Single Mol.* **2**, 255–260 (2001).
15. Evans, R. E., Sipahigil, A., Sukachev, D. D., Zibrov, A. S. & Lukin, M. D. Narrow-linewidth homogeneous optical emitters in diamond nanostructures via silicon ion implantation. *Phys. Rev. Appl.* **5**, 044010 (2016).
16. Rogers, L. J. et al. Multiple intrinsically identical single-photon emitters in the solid state. *Nat. Commun.* **5**, 4739 (2014).
17. Tamura, S. et al. Array of bright silicon-vacancy centers in diamond fabricated by low-energy focused ion beam implantation. *Appl. Phys. Express* **7**, 115201 (2014).
18. Tzeng, Y. K. et al. Vertical-substrate MPCVD epitaxial nanodiamond growth. *Nano Lett.* **17**, 1489–1495 (2017).
19. Crane, M. J. et al. HPHT molecular doping of nanodiamond. *Sci. Adv.* **5**, eaau6073 (2019).
20. Crane, M. J. et al. Photothermal effects during nanodiamond synthesis from a carbon aerogel in a laser-heated diamond anvil cell. *Diam. Relat. Mater.* **87**, 134–142 (2018).
21. Pauzauskie, P. J. et al. Synthesis and characterization of a nanocrystalline diamond aerogel. *Proc. Natl Acad. Sci. USA* **108**, 8550–8553 (2011).
22. Schroder, T. et al. Scalable focused ion beam creation of nearly lifetime-limited single quantum emitters in diamond nanostructures. *Nat. Commun.* **8**, 15376 (2017).
23. Park, S. et al. Facile diamond synthesis from lower diamondoids. *Sci. Adv.* **6**, eaay9405 (2020).
24. Mao, H. K., Xu, J. & Bell, P. M. Calibration of the ruby pressure gauge to 800 kbar under quasi-hydrostatic conditions. *J. Geophys. Res.* **91**, 4673–4676 (1986).
25. Goncharov, A. F. et al. Laser heating in diamond anvil cells: developments in pulsed and continuous techniques. *J. Synchrotron Radiat.* **16**, 769–772 (2009).
26. Akahama, Y. & Kawamura, H. Pressure calibration of diamond anvil Raman gauge to 310GPa. *J. Appl. Phys.* **100**, 043516 (2006).
27. Alkahtani, M., Lang, J., Naydenov, B., Jelezko, F. & Hemmer, P. Growth of high-purity low-strain fluorescent nanodiamonds. *ACS Photonics* **6**, 1266–1271 (2019).
28. Choi, D. Phase transformation in thin tungsten films during sputter deposition. *Microelectron. Eng.* **183-184**, 19–22 (2017).
29. Gromov, D. G. & Gavrilov, S. A. Heterogeneous melting in low-dimensional systems and accompanying surface effects. In *Thermodynamics—Physical Chemistry of Aqueous Systems*. (ed. Moreno-Piraján, J. C.) https://www.intechopen.com/chapters/20159 (2011).
30. Grudinkin, S. A., Feoktistov, N. A., Bogdanov, K. V., Baranov, A. V. & Golubev, V. G. Photoluminescence of germanium-vacancy color centers in diamond particles obtained by chemical vapor deposition. *Phys. Solid State* **62**, 919–925 (2020).
31. Lal, S., Dallas, T., Yi, S., Gangopadhyay, S. & Holtz, M. Defect photoluminescence in polycrystalline diamond films grown by arc-jet chemical-vapor deposition. *Phys. Rev. B* **54**, 13428 (1996).
32. Lyapin, S. G., Ilichev, I. D., Novikov, A. P., Davydov, V. A. & Agafonov, V. N. Study of optical properties of the NV and SiV centres in diamond at high pressures. *Nanosyst. Phys. Chem. Math.* **9**, 55–57 (2018).
33. Czelej, K., Zemła, M. R., Śpiewak, P. & Kurzydłowski, K. J. Quantum behavior of hydrogen-vacancy complexes in diamond. *Phys. Rev. B* **98**, 235111 (2018).
34. Tolochko, B. P. et al. Investigation of adamantane–diamond transformation. The radical mechanism of the formation of diamond nanoparticles under shock-wave action on adamantane. *J. Struct. Chem.* **57**, 1469–1476 (2017).
35. Zeng, Z. et al. Preservation of high-pressure volatiles in nanostructured diamond capsules. *Nature* **608**, 513–517 (2022).

36. Pezzagna, S., Rogalla, D., Wildanger, D., Meijer, J. & Zaitsev, A. Creation and nature of optical centres in diamond for single-photon emission—overview and critical remarks. *New J. Phys.* **13**, 035024 (2011).
37. Prins, J. F. C^+-damaged diamond: electrical measurements after rapid thermal annealing to 500°C. *Diam. Relat. Mater.* **10**, 463–468 (2001).
38. Henkelman, G. & Jónsson, H. Improved tangent estimate in the nudged elastic band method for finding minimum energy paths and saddle points. *J. Chem. Phys.* **113**, 9979 (2005).
39. Henkelman, G. A climbing image nudged elastic band method for finding saddle points and minimum energy paths. *J. Chem. Phys.* **113**, 9901–9904 (2000).
40. Kresse, G. & Hafner, J. Ab initio molecular dynamics for liquid metals. *Phys. Rev. B Condens. Matter* **47**, 558–561 (1993).
41. Kresse, G. & Hafner, J. Ab initio molecular-dynamics simulation of the liquid-metal-amorphous-semiconductor transition in germanium. *Phys. Rev. B Condens. Matter* **49**, 14251–14269 (1994).
42. Kresse, G. & Furthmüller, J. Efficiency of ab-initio total energy calculations for metals and semiconductors using a plane-wave basis set. *Comput. Mater. Sci.* **6**, 15–50 (1996).
43. Kresse, G. & Furthmüller, J. Efficient iterative schemes for ab initio total-energy calculations using a plane-wave basis set. *Phys. Rev. B* **54**, 11169–11186 (1996).
44. Kuate Defo, R., Kaxiras, E. & Richardson, S. L. How carbon vacancies can affect the properties of group IV color centers in diamond: a study of thermodynamics and kinetics. *J. Appl. Phys.* **126**, 195103 (2019).
45. Voter, A. F. Introduction to the kinetic Monte Carlo method in *Radiation Effects in Solids* (Springer, 2007).
46. Wilkes, G. C., Deng, X., Choi, J. J. & Gupta, M. C. Laser annealing of TiO_2 electron-transporting layer in perovskite solar cells. *ACS Appl. Mater. Interfaces* **10**, 41312–41317 (2018).
47. Kwon, H. et al. Ultra-short pulsed laser annealing effects on MoS_2 transistors with asymmetric and symmetric contacts. *Electronics* **8**, 222 (2019).
48. Mills, G., Jonsson, H. & Schenter, G. K. Reversible work transition state theory—application to dissociative adsorption of hydrogen. *Surf. Sci.* **324**, 305–337 (1995).
49. Virtanen, P. et al. SciPy 1.0: fundamental algorithms for scientific computing in Python. *Nat. Methods* **17**, 261–272 (2020).
50. Milman, V. V. et al. Free energy and entropy of diffusion by ab initio molecular dynamics: alkali ions in silicon. *Phys. Rev. Lett.* **70**, 2928–2931 (1993).
51. Vineyard, G. H. Frequency factors and isotope effects in solid state rate processes. *J. Phys. Chem. Solids* **3**, 121–127 (1957).

Acknowledgements

This work is supported by the Moore Foundation under grant No. 4309, Thorlabs, and the U.S. Department of Energy (DOE), Office of Science, Basic Energy Sciences, Materials Sciences and Engineering Division, under contract No. DE-AC02-76SF00515 (DAC experiments and theoretical simulations). The simulation work used resources of the National Energy Research Scientific Computing Center (NERSC), a DOE Office of Science User Facility operated under Contract No. DE-AC02-05CH11231. We acknowledge the Stanford Nanofabrication Facility (SNF) and SNSF for sample preparation and characterization. M.F. acknowledges DOE FES FWP100182 for the setup of the nanosecond laser heating.

Author contributions

Y.T. and S.C. conceived the research. Y.T. and F.K. built up the optical systems and carried out the experiments and data analysis. F.K. carried out the high-pressure experiments under the supervision of Y.Lin, C.J., X.C. and T.P.D. carried out the theoretical calculations. Y.Liu assisted in sputtering the metal film. M.F. assisted in the nanosecond laser-heating experiment in a DAC. W.L.M., R.C.E. and Y.C. supported the experimental equipment. S.P. assisted in the initial high-pressure experiment and M.H. helped additional high-pressure experiments. Y.T., F.K., C.J., Y.Lin and S.C. wrote the paper. All authors have given approval to the final version of the manuscript.

Competing interests

The authors declare no competing interests.

Additional information

Supplementary information The online version contains supplementary material available at https://doi.org/10.1038/s41467-024-51523-2.

Correspondence and requests for materials should be addressed to Yu Lin or Steven Chu.

Peer review information *Nature Communications* thanks Yuto Makino, Peter Pauzauskie and the other anonymous reviewers for their contribution to the peer review of this work. A peer review file is available.